Available online at www.sciencedirect.com

jmr&t Journal of Materials Research and Technology

www.jmrt.com.br

Original Article

Synergistic effects of WC nanoparticles and MC nanoprecipitates on the mechanical and tribological properties of $Fe_{40}Mn_{40}Cr_{10}Co_{10}$ medium-entropy alloy

Jianying Wang[a], *Hailin Yang*[a,*], *Zhilin Liu*[b], *Ruidi Li*[a], *Jianming Ruan*[a], *Shouxun Ji*[c]

[a] *State Key Laboratory of Powder Metallurgy, Central South University, Changsha 410083, China*
[b] *College of Mechanical and Electrical Engineering, Central South University, Changsha 410083, China*
[c] *Institute of Materials and Manufacturing, Brunel University London, Uxbridge, Middlesex UB8 3PH, United Kingdom*

ARTICLE INFO

Article history:
Received 27 November 2018
Accepted 19 June 2019
Available online 4 July 2019

Keywords:
Composites
Medium entropy alloys (MEAs)
Microstructure
Mechanical property
Tribological property

ABSTRACT

The synthesis of $Fe_{40}Mn_{40}Cr_{10}Co_{10}$/WC composites by a combination of ball milling and spark plasma sintering is reported and corresponding mechanical and tribological properties of these composites are investigated. Compared with the $Fe_{40}Mn_{40}Cr_{10}Co_{10}$ MEA (medium entropy alloy), the addition of 10 vol.% WC nanoparticles led to an increase in the compressive strength and hardness from 1.571 GPa and 320 HV to 2.324 GPa and 788 HV, respectively. Meanwhile, tribological tests demonstrated that the friction coefficient, wear depth and width of the composite decreased in comparison with $Fe_{40}Mn_{40}Cr_{10}Co_{10}$ MEA. Load transfer effect, thermal mismatch mechanism, Orowan strengthening and grain refinement resulting from synergistic effects between *ex-situ* WC nanoparticles and *in-situ* $M_{23}C_6$ nanoprecipitates are responsible for the improvement in mechanical properties, especially thermal mismatch mechanism and grain refinement. In addition, the enhancement in tribological properties is also ascribed to these synergistic effects.

1. Introduction

High-entropy alloys (HEAs) and medium-entropy alloys (MEAs), which consist of multiple equiatomic or near-equiatomic elements, are relatively-new concepts developed to replace conventional alloys [1,2]. More attention has been paid to MEAs owing to their superior ductility and fracture toughness [3–6]. The metastable $Fe_{80-x}Mn_xCr_{10}Co_{10}$ (at.%) alloy is one of the novel quaternary MEAs to offer outstanding engineering strain (46–73% elongation) [7]. A representative microstructure of as-cast $Fe_{40}Mn_{40}Cr_{10}Co_{10}$ MEA [8] consists of a FCC single phase that is responsible for the extraordinary elongation of 57.7%. However, its relatively low yield strength of 213 MPa and hardness of 143 HV are insufficient to meet the demands of some structural applications. Over the years, various strengthening approaches have been introduced to

* *Corresponding author.*
E-mail: y-hailin@csu.edu.cn (H. Yang).
https://doi.org/10.1016/j.jmrt.2019.06.031

enhance the mechanical properties of MEAs, which roughly include grain refinement [9,10] and precipitation strengthening [11,12].

Taking the simple solid solution nature of MEAs in consideration, these alloys have suitable matrices for particle-reinforced metal matrix composite (PRMMC) with improved mechanical and tribological properties, especially via reinforcement of nanoparticles. The strengthening in PRMMCs is usually complicated on account of the comprehensive effect of multiple strengthening mechanisms. The possible mechanisms include [13–21]: (1) the load transfer effect, (2) grain refinement strengthening, (3) Orowan strengthening, (4) dislocation strengthening caused by the discrepancy in the coefficient of thermal expansion (CTE), and (5) precipitation strengthening. In fact, all the strengthening effects originate from the synergistic effect of *ex-situ* reinforcements and *in-situ* precipitates (if there are precipitates in the composites). For example, *in-situ* δ′ (Al_3Li) particles were dispersed homogenously in the TiB_2/Al-Li-Cu composite. Most of the TiB_2 particles agglomerating along the grain boundaries and the fine δ′ (Al_3Li) precipitates distributing within grains promoted the improvement of mechanical properties [22]. Similarly, Al-B_4C composites with dispersion of nano-sized Al_3Sc precipitates by the addition of Sc exhibited the highest strength at room temperature and the excellent stability in the strength up to 673 K (400 °C), compared with the Al-B_4C composites [23]. In addition, MC-type carbide precipitates have attracted a lot interesting of investigations. The fine $M_{23}C_6$ carbides precipitating at grain boundaries in nickel-based superalloys demonstrated a beneficial effect on stress rupture lives [24]. Shen et al. [25] investigated the effect of TiC on the microstructure and fracture behavior of particle-reinforced Inconel 625 composites and showed that the uniform distribution of precipitated MC (M = Nb, Ti, and Mo) phases enhanced the mechanical properties of the TiC/Inconel 625 composite. For MEAs and HEAs, the addition of 10 vol.% SiC particles facilitated the development of *in situ* formed $M_{23}C_6$ nanoprecipitates from the $Fe_{40}Mn_{40}Cr_{10}Co_{10}$ MEA [26]. A uniform distribution of SiC and $M_{23}C_6$ particles delivered ultimate compressive strength up to 2513 MPa. Elements Ti and C were doped into the FeCoCrNiMn HEA, and TiC nanoparticles and a small amount of $M_{23}C_6$ and M_7C_3 (M = Cr, Mn, Fe) carbides resulted in excellent mechanical properties [27]. Clearly, the synergistic effects of *ex-situ* reinforcements and *in-situ* MC precipitates can be considered as an advisable method in counterpart with the simple particle dispersion strengthening.

Tungsten carbide (WC) has been used as one of the preferred reinforcement phases in MMCs of Al- [28], Fe- [29,30], and Cu-base alloys [31] because of its high hardness, chemical stability, and wear resistance [32,33]. In this study, $Fe_{40}Mn_{40}Cr_{10}Co_{10}$ MEA matrix composites reinforced with WC nanoparticles were prepared by spark plasma sintering (SPS). The effects of the WC nanoparticles and MC-type nanoprecipitates on the mechanical and tribological properties of $Fe_{40}Mn_{40}Cr_{10}Co_{10}$/WC composites were investigated. The discussion focuses on the strengthening mechanisms and the improvement in tribological performance.

2. Experimental

2.1. Materials preparation

Water-atomized $Fe_{40}Mn_{40}Cr_{10}Co_{10}$ (in atomic ratios) MEA powder was used as the starting material, with the average particle size being 5–15 μm. The concentration of WC nanoparticles with a size of 100–200 nm was 10 vol.%, corresponding to the FM-W10 composite (herein, the $Fe_{40}Mn_{40}Cr_{10}Co_{10}$ and the $Fe_{40}Mn_{40}Cr_{10}Co_{10}$/10 vol.% WC, denoted as the FM and the FM-W10, respectively). WC and the FM powder were mixed by planetary ball milling to obtain uniform mixed powder. The milling was conducted at a speed of 400 rpm for 6 h with a 3:1 weight ratio of ball to powder. Alcohol was used as the process control agent (PCA) to avoid cold welding and prevent the powder from oxidation. The mixed powders were subsequently consolidated by SPS in a 40-mm-inner-diameter graphite die at 1100 °C for 10 min with a uniaxial pressure of 40 MPa.

2.2. Material characterization

CALPHAD simulations of the solidification pathway during sintering were performed using JMatPro. Phase identification and microstructural characterization were carried out using X-ray diffraction (Rigaku X-2000, XRD) and scanning electron microscopy (FEI nano 230 field emission, SEM) equipped with energy dispersive spectrometry (EDS). Electron backscattered diffraction (EBSD) was conducted using a Hitachi S-3400 N SEM instrument equipped with an HKL-EABS system to examine the grain size and lattice-preferred orientations. Transmission electron microscopy (TEM) with selected-area electron diffraction (SAED) was performed with a Tecnai G2 F20 microscope operated at 200 kV. The specimens for TEM were prepared by grinding–polishing to produce thin foils of 50 μm thickness, followed by ion beam thinning.

2.3. Mechanical property test

The compressive properties of the FM MEA and the FM-W10 composite were assessed by an Instron 3369 universal testing machine with a cross head speed of 1 mm/min. The hardness of the FM MEA and the FM-W10 composite was measured by a HVS-5 hardness tester. Also, a nanoindentation test was performed to measure the elastic modulus employing UNHT equipment. All the reported data were the average of at least five specimens.

2.4. Tribological property test

Dry sliding wear tests of the FM MEA and the FM-W10 composite were carried out with an HRS-2 M roller friction wear tester at room temperature. A counter-face ball with a diameter of 5 mm was made of Si_3N_4. The testing time, load and sliding speed were set at 5 min, 10 N, and 600 rpm, respectively. The element composition on the surface after the tribological test was estimated using X-ray photoelectron spectroscopy (XPS) (K-ALPHA X-rays, Thermo Fisher Scientific) with an X-ray source operated at 6 mA and 12 kV.

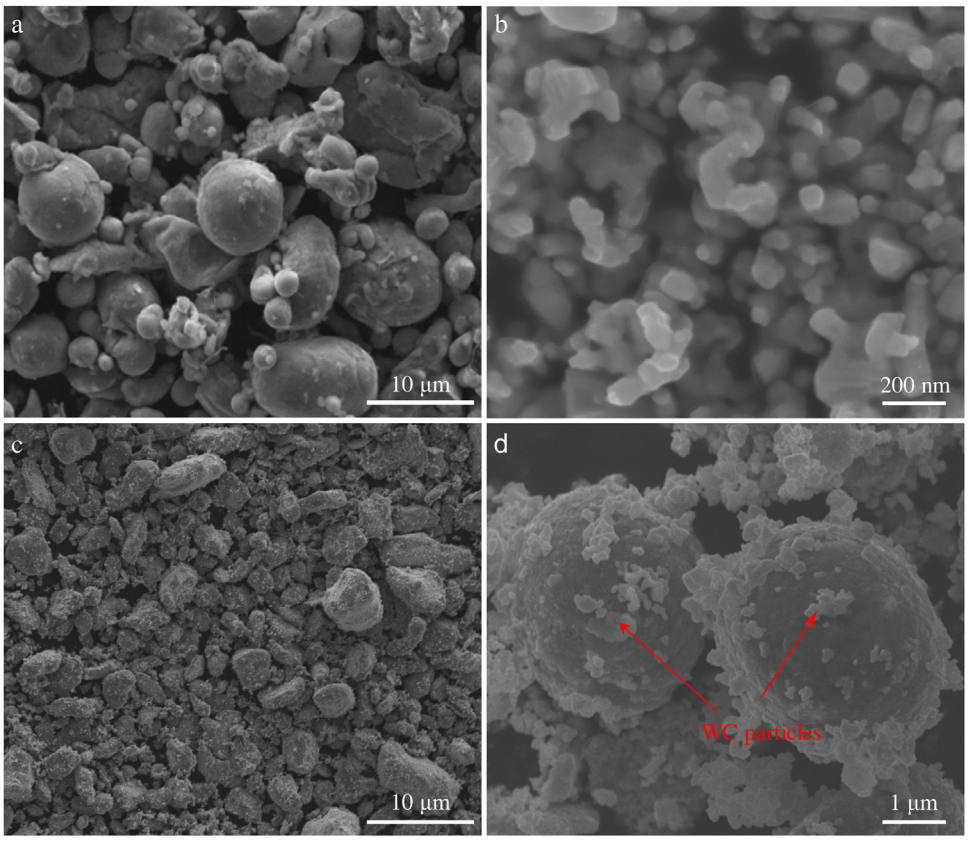

Fig. 1 – Typical SEM micrographs showing (a) $Fe_{40}Mn_{40}Co_{10}Cr_{10}$ MEA powder, (b) WC nanoparticles, (c) and (d) $Fe_{40}Mn_{40}Co_{10}Cr_{10}$/10 vol.% WC mixed powder, showing relatively homogeneous distribution of WC nanoparticles. Red arrows in (d) indicate a few WC agglomerates in the micron size range. (For interpretation of the references to colour in this figure legend, the reader is referred to the web version of this article).

3. Results

3.1. *Morphologies of raw material and mixing powder*

The morphologies of the FM MEA, WC and ball-milled powder are shown in Fig. 1. The raw water atomization the FM MEA powder mainly displayed an irregular shape and some of them were close to spherical (Fig. 1a). The results in Fig. 1b shows that the WC nanoparticles presented with a relatively homogeneous size distribution and the sizes ranged from 100 to 200 nm. After ball milling of 6 h, WC nanoparticles were assembled slightly and distributed evenly on the FM MEA powder, and only a few of WC nanoparticles was found as agglomerates in micron size ranges, as shown in Fig. 1c and d.

3.2. *Microstructure characterization*

The SEM/BSE micrographs in Fig. 2 show the general microstructure of the FM MEA and the FM-W10 composite processed by SPS. The FM alloy exhibited a homogenous single phase with some pores as marked by the arrows in Fig. 2a. The FM alloy with the addition of WC nanoparticles shows a relatively complex microstructure. Bright WC phases were uniformly distributed, and a certain degree of agglomeration of the WC phases, which could be attributed to the density difference between the matrix and WC, existed in the FM-W10 composite. From the SEM image at higher magnification in Fig. 2c, nano-sized precipitates presented spherical or irregular shape of within grains (red lines) and along grain boundaries (yellow lines). Elemental mapping on the selected area of precipitates was carried out by SEM/EDX. As shown in Fig. 3, the Fe, Mn and Co elements were distributed uniformly in the matrix grains. However, Cr and C were mainly segregated to form precipitate phases. Considering the high affinity of Cr toward C, it is believed that the chromium carbide formed by the reaction with carbon during SPS processing. This is similar to the phenomenon observed previously [29,34,35]. Fig. 2d gives the XRD spectra of the FM MEA and the FM-W10 composite. The FM MEA showed a single-phase FCC structure, which is in good agreement with the previous study [8]. The diffraction spectrum of the FM-W10 composite also showed the existence of the peaks of WC and $M_{23}C_6$ type carbides, indicating that the chromium carbide was $M_{23}C_6$ structure in this preliminary work.

The mean grain size and grain orientation of the as-SPSed FM MEA and FM-W10 composite were studied using EBSD to understand the effect of WC nanoparticles on the grain refinement of the FM MEA. As indicated by the EBSD maps in Fig. 4, with the addition of WC nanoparticles, an obvious grain refinement and much fewer pores were observed in the composite. The average grain size of the FCC phase was decreased

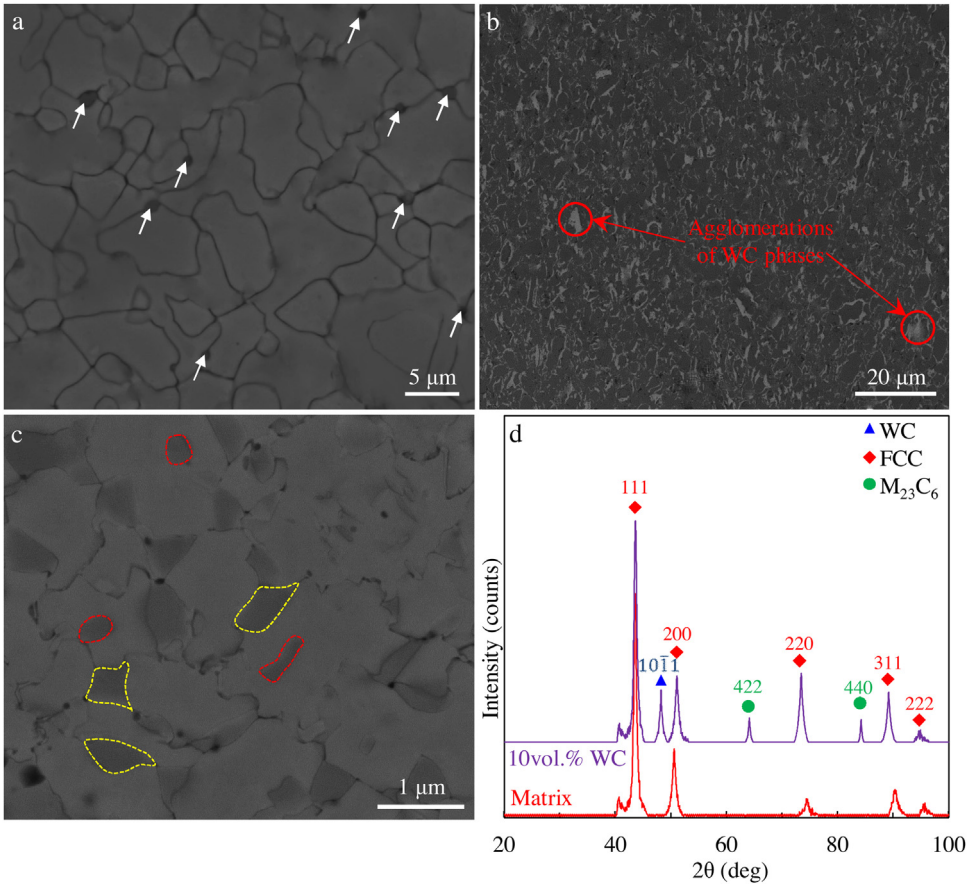

Fig. 2 – Backscattered SEM micrographs showing (a) the microstructure of $Fe_{40}Mn_{40}Cr_{10}Co_{10}$ MEA, (b) and (c) $Fe_{40}Mn_{40}Cr_{10}Co_{10}$/10 vol.% WC composite; (d) X-ray diffraction patterns of $Fe_{40}Mn_{40}Cr_{10}Co_{10}$ MEA and its composite reinforced by WC nanaparticles with clear WC, FCC and $M_{23}C_6$ peaks. Red arrows in (b) indicate a few agglomerations of WC phases. Red and yellow lines in (c) exhibit that precipitates are distributed within grains and along grains boundaries, respectively. (For interpretation of the references to colour in this figure legend, the reader is referred to the web version of this article).

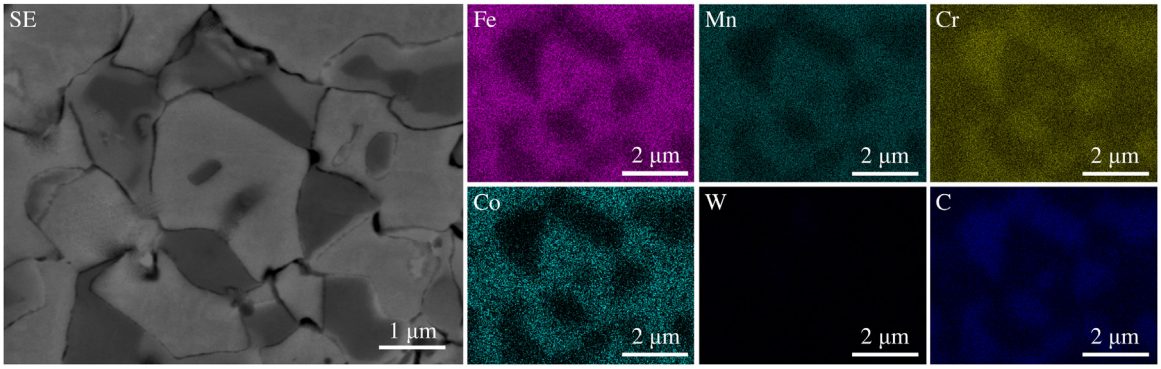

Fig. 3 – SEM-EDS mapping images showing the element distribution of $Fe_{40}Mn_{40}Cr_{10}Co_{10}$/10 vol.% WC composite.

from 4.20 μm in the FM MEA to 1.61 μm in the FM-W10 composite. The average size of the WC shown in Fig. 4d was 0.54 μm, much higher than that of the raw WC nanoparticles (100–200 nm in size). This might be attributed to two reasons: one is the aggregation of some WC nanoparticles that occurred during materials mixing, and the other is that WC nanoparticles were aggregated further during the sintering process. The inverse pole figures of the FCC phase shown as inserts in Fig. 4 confirmed that the FCC grains had no obvious preferred orientation in the FM MEA and the FM-W10 composite.

TEM images and the corresponding selected area electron diffractions patterns (SADPs) of the FM MEA and the FM-W10

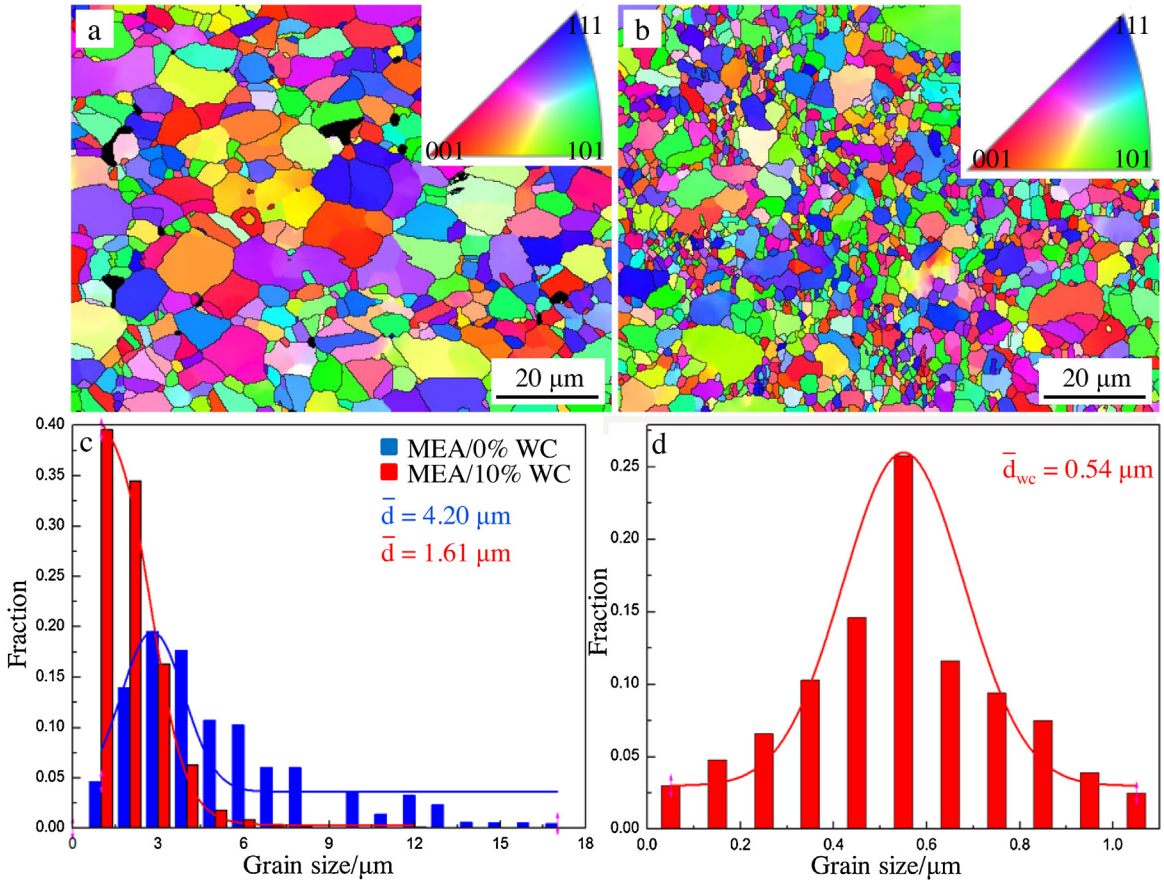

Fig. 4 – EBSD mapping-based microstructures showing the variation of grain sizes of (a) $Fe_{40}Mn_{40}Cr_{10}Co_{10}$ MEA, (b) $Fe_{40}Mn_{40}Cr_{10}Co_{10}$/10 vol.% WC composite; (c) and (d) Distribution of average grain sizes of FCC and WC phases, respectively. The inserts in (a) and (b) are the inverse pole figures (IPFs) of the FCC phase in the alloy.

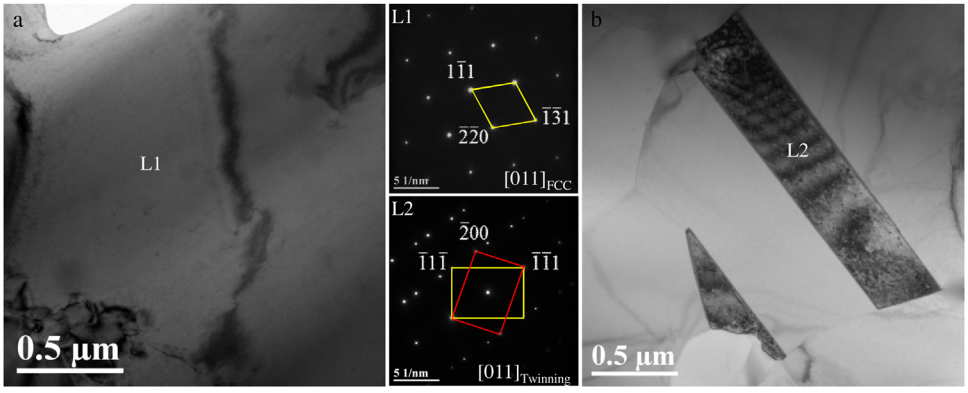

Fig. 5 – TEM BF micrographs of $Fe_{40}Mn_{40}Cr_{10}Co_{10}$ MEA, including (a) BF and SADP (L1) showing FCC structure of $Fe_{40}Mn_{40}Cr_{10}Co_{10}$ MEA; (b) BF and SADP (L2) showing annealing twins.

composite are shown in Figs. 5 and 6. A simple FCC phase was seen in the microstructure of the FM MEA, but other phases were not observed. Also, dark WC phases with sizes of 150 to 500 nm were indicated by the yellow line in Fig. 6a. As expected, some nanoprecipitates were also observed within grains and along grain boundaries in Fig. 6b. The results were consistent with the SEM observation shown in Fig. 2c. Moreover, a twinning phase was also observed in Figs. 5b and 6c, confirming that these systems of MEA and composite had a low stacking fault energy in the interval of $18 < \gamma_{SFE} < 45\ MJ\ m^{-2}$ [36]. The corresponding TEM SADPs from Fig. 6a, b, and c are shown in Fig. 6(L1-L2) to (L3-L4). Furthermore, CALPHAD simulations of solidification pathway of the FM and the FM-W10 during sintering were performed using JMatPro software, as

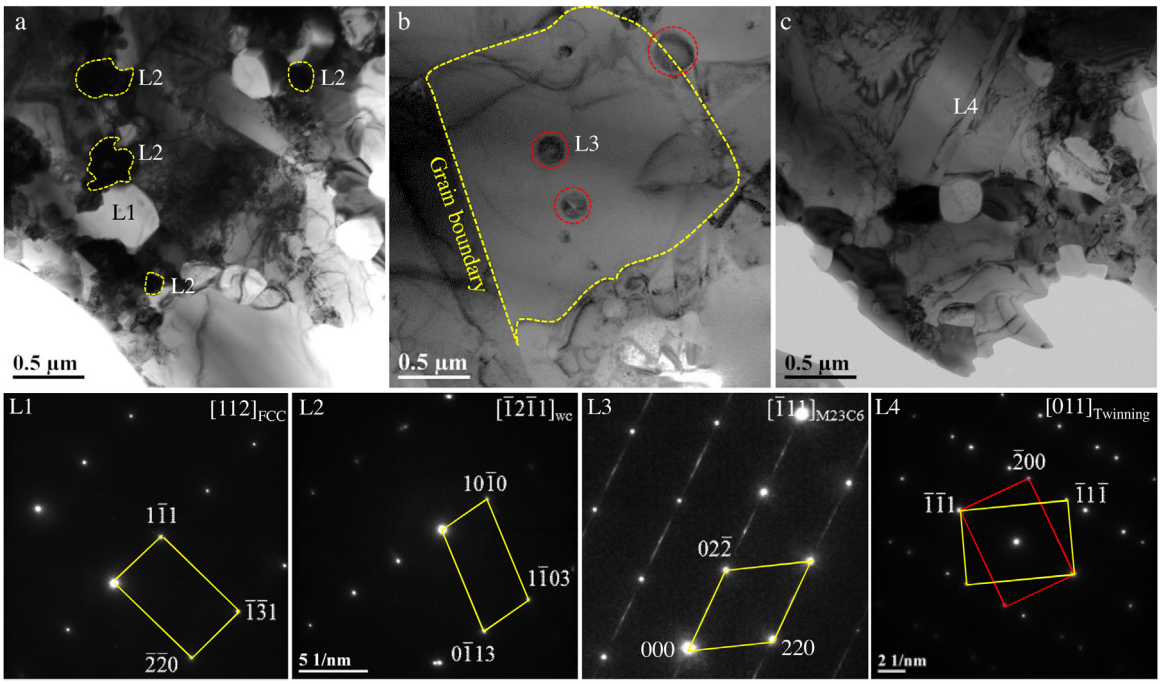

Fig. 6 – TEM BF micrographs of $Fe_{40}Mn_{40}Cr_{10}Co_{10}$ /10 vol.% WC composite, including (a) WC nanoparticles (padding between adjacent grains),(b)$M_{23}C_6$ nanoprecipitates (within grain and along grain boundary) and (c) twinning phase; (L1)-(L2),(L3) and (L4) showing SAD patterns corresponding to the areas marked by (L1)-(L2), (L3) and (L4) in (a), (b) and (c), respectively. (For interpretation of the references to color in the text, the reader is referred to the web version of this article).

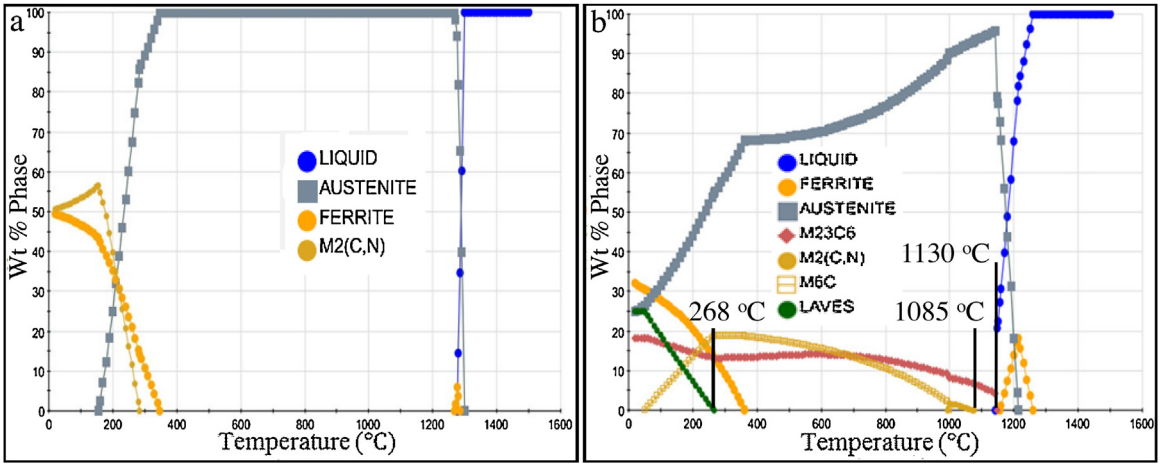

Fig. 7 – Solidification pathway of the potential phases in (a) $Fe_{40}Mn_{40}Cr_{10}Co_{10}$ MEA and (b) $Fe_{40}Mn_{40}Cr_{10}Co_{10}$/10 vol.% WC composite during sintering using CALPHAD simulation.

seen in Fig. 7a and b. An FCC phase was predicted to become stable in the FM alloy. Also, CALPHAD calculation showed that potential phases, i.e., $M_{23}C_6$ and M_2(C,N), would be developed from 1130 °C and 1085 °C, respectively. However, the M_2(C,N) phase was not detected by XRD and TEM examination, which might be attributed to the decomposition of M_2(C,N) phase from 268 °C. Similar experimental results have already been reported in the $FeCoCrNiW_{0.3}$ +0.5 at.% C alloy [37], C-doped $Fe_{40.4}Ni_{11.3}Mn_{34.8}Al_{7.5}Cr_6$ HEAs [38], and WC-doped FeCoCrNi alloy [39]. In this study, the potential source of C atoms came from two aspects, carbon contamination of SPS graphite and *ex situ* WC nanoparticles. However, under the same experimental conditions, no nanoprecipitates appeared in the FM MEA, as shown in Figs. 2a and 6. Thus, the formation of nanoprecipitates in this study might not be attributed to the carbon contamination in the MEA during SPS processing, but it was probably owing to the decomposition of WC nanoparticles. In addition, several studies about the thermal stability of WC and its chemical interaction with steel suggested that the formation of W_2C [40–45] and M_6C (M = W, Fe) [40,46–48] was expected to occur at temperatures above 1100 °C. For example, Lou et al. [40] indicated that matrix compositions had a strong

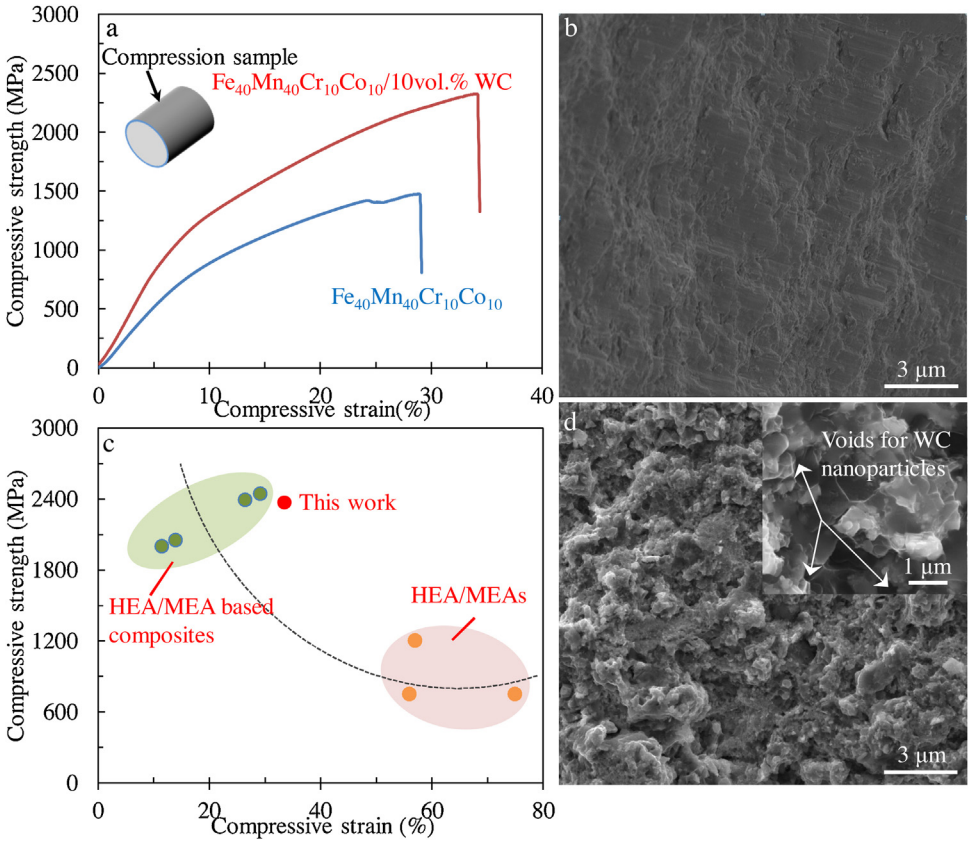

Fig. 8 – Compressive stress-strain curves of $Fe_{40}Mn_{40}Cr_{10}Co_{10}$ MEA and $Fe_{40}Mn_{40}Cr_{10}Co_{10}$/10 vol% WC composite in (a); Fracture surfaces of the as-sintered $Fe_{40}Mn_{40}Cr_{10}Co_{10}$ with (b) 0 and (d) 10 vol.% WC. Voids of the post-deformed samples are highlighted by the white arrows in (d); (c) comparison of strength vs deformation of typical HEA/MEAs [50–52] and HEA/MEA based composites [26,27,53,54].

influence on the formation of W_2C and M_6C phases because of the dissolution of WC particles, especially for Co, Fe, Cr, and Mo elements. Rajaei et al. [49] suggested that WC decomposed into W_2C at ~1450 °C under a pressure of 30 MPa. Similarly, $M_{23}C_6$-type and M_7C_3-type carbides could be developed in the microstructure of as-SPSed $(FeCoCrNi)_{1-x}(WC)_x$ HEA composites [39], Zhou et al. believed that these MC-type carbides resulted from the diffusion and reaction of W and C with the matrix and overlooked the contamination of SPS graphite. However, carbon contamination from the SPS graphite die mold in this study could not be fully avoided. Wang et al. [46] found that the graphite die had a function of carburization, which could compensate the sintered body for the lack of carbon. Thus, this raises an open question regarding the origin of carbide formation.

3.3. *Mechanical properties*

Fig. 8 shows the compressive performance curves of the FM MEA and the FM-W10 composite and their corresponding fracture morphologies. The detailed compressive properties and Vickers hardness are listed in Table 1. It is seen that the FM MEA exhibited a lower Vickers hardness of 320 HV and the compressive strength of 1.571 GPa, but it presented a relatively high compressive strain of 28.5%. With the addition of 10 vol.% WC, the Vickers hardness and the ultimate compressive strength of the FM-W10 composite increased to 788 HV and 2.324 GPa, respectively, with a slight increase in the compressive strain to 33.9%. the FM MEA showed a single slip fracture surface in Fig. 8b, while the fracture surface of the FM-W10 was a typical ductile-brittle mode in Fig. 8d. Moreover, there were many voids remained on the surface of the composite after WC nanoparticles were pulled out. The mechanical properties of similar materials for comparison are also shown in Fig. 8c. This figure shows that the comprehensive mechanical properties of the composite exceed the properties of medium- and high-entropy alloys [50–52] and their based composites reported in literatures [26,27,53,54].

TEM micrographs of the sintered FM MEA and the FW-W10 composite after the compress deformation are shown in Fig. 9. A high density of dislocations could be observed in Fig. 9a. In addition, some narrow deform twins (marked by the red arrows) in Fig. 9b with a width of tens of nanometers were observed. The interaction of dislocations with WC nanoparticles and $M_{23}C_6$ nanoprecipitates in the FM-W10 composite could be seen in Figs. 9c and d. The nanoparticles and nanoprecipitates blocked a large amount of dislocations to form the pileup of dislocations. It is also noted that WC nanoparticles and $M_{23}C_6$ nanoprecipitates were not plastically sheared by gliding dislocations during plastic deformation. These

Table 1 – Summary of mechanical properties obtained during compressive and hardness testing.

	Yield strength (GPa)	Compressive strength (GPa)	Compressive strain(%)	Vickers hardness
MEA	0.488	1.571	28.5	320
MEA/10 vol.% WC	0.827	2.324	33.9	788

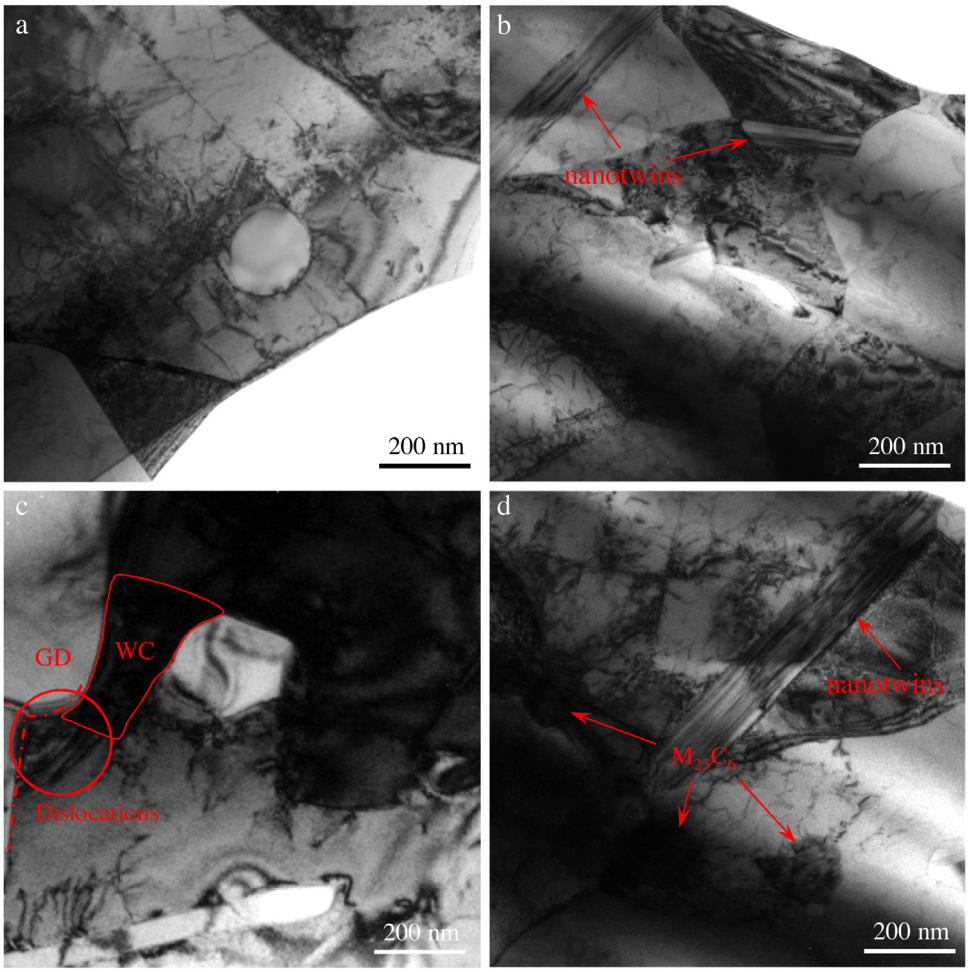

Fig. 9 – TEM micrographs of the sintered FM MEA (a and b) and FW-W10 composite (c and d) after the compress deformation, (a) a high density of dislocations and (b) deformation nanotwins in FM MEA. (c) and (d) the interaction of dislocations with WC nanoparticles and nanoprecipitates. (For interpretation of the references to color in the text, the reader is referred to the web version of this article).

non-shearable WC nanoparticles and $M_{23}C_6$ nanoprecipitates accounted for high strength of the FM-W10 composite. On top of these, nanotwins were also observed in the FM-W10 composite. Twin boundaries associated with nanotwins could provide an exceptional ductility by blocking the motion of dislocations. This was one reason why the compressive strain of the FM-W10 composite did not decrease. Another reason was that the obvious decrease in grain size was shown in Fig. 4. In the present work, we only focus on the effects of WC nanoparticles and MC nanoprecipitates on the mechanical and tribological properties. WC nanoparticles and MC nanoprecipitates were sufficiently identified by the indexed TEM diffraction patterns in Fig. 6. However, STEM elemental mapping can provide extra chemical/physical basis of the processes used in the as-sintered composite.

3.4. *Tribological property*

The 3D optical wear track and the corresponding 2D cross-section depth profile of the FM MEA and the FM-W10 composite under 10 N load are shown in Fig. 10. As expected, the wear track of the FM MEA was deeper and wider than that of the FM-W10 composite. The tracks of the FM MEA were 2.20 times deeper and 1.28 times wider than those of the FM-W10 composite. Meanwhile, the friction coefficient was 0.6 for the FM MEA, compared with 0.28 for the FM-W10 composite. The reduced depth, width, and friction coefficient demonstrated that the FM-W10 composite had a better tribological property than the FM MEA.

Figs. 11 and 12 show the SEM morphologies of the worn-out surfaces of the FM MEA and the FM-W10 composite. Some

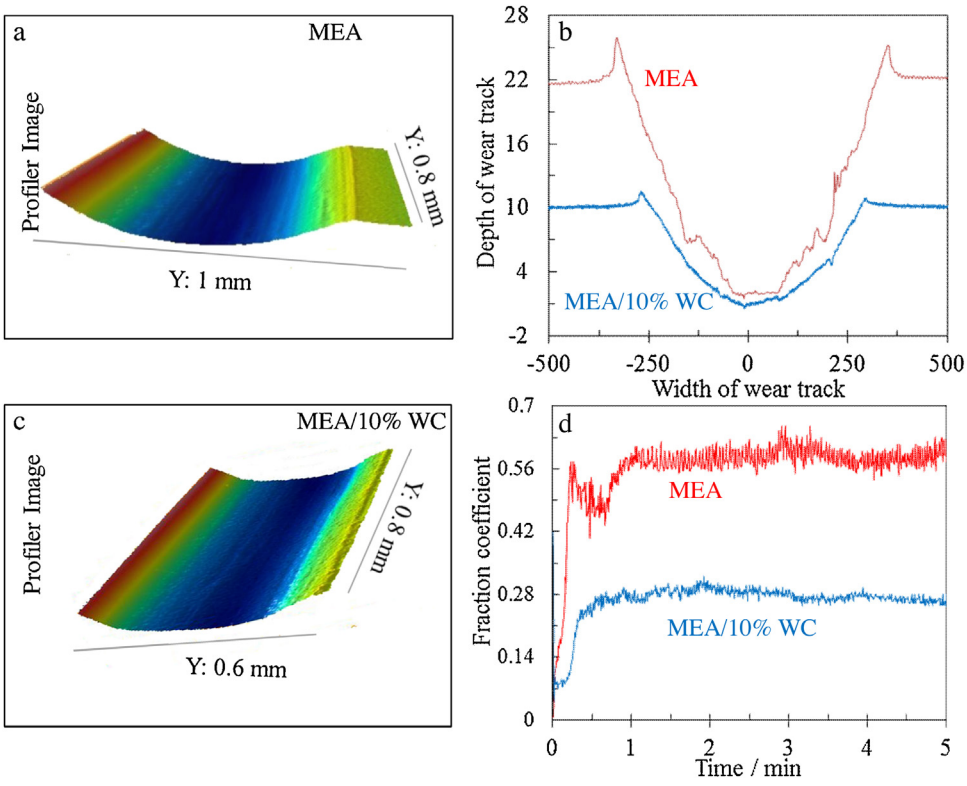

Fig. 10 – (a) and (c) 3D optical wear track of $Fe_{40}Mn_{40}Cr_{10}Co_{10}$ MEA and $Fe_{40}Mn_{40}Cr_{10}Co_{10}$/10 vol% WC composite under 10 N load; (b) Cross-section depth profile of $Fe_{40}Mn_{40}Cr_{10}Co_{10}$ MEA and $Fe_{40}Mn_{40}Cr_{10}Co_{10}$/10 vol% WC composite; (d) Fraction coefficient of $Fe_{40}Mn_{40}Cr_{10}Co_{10}$ MEA and $Fe_{40}Mn_{40}Cr_{10}Co_{10}$/10 vol% WC composite from the 10 N load test condition.

micro-ploughing was obviously present in the FM MEA, as shown in Fig. 11a. From the SEM image at higher magnification in Fig. 11b, the wear particles were clearly visible inside the wear track of the FM MEA. According to the EDS results in Fig. 11b1 and b2, the matrix grains were oxidized during the tribological test and the wear particles were identified as metallic oxides. These characteristics suggested that the main wear mechanism of the FM MEA included abrasive wear and oxidation wear. Compared with the FM MEA, a smooth worn surface could be found in the FM-W10 composite (Fig. 12a). Only a few of slight friction marks along the sliding direction were found. This showed that the uniformly dispersed WC limited the plastic deformation of the matrix and played a positive role in reducing the micro-ploughing. From the micrographs in Fig. 12b, although some abrasion could be observed, a small part of matrix removals and WC removals was also observed. The fact that only a few particles were being torn out from the matrix confirmed the existence of a strong interfacial bonding between the matrix and WC. Elemental mapping was further carried out by SEM/EDS. The results in Fig. 12b1–b7 confirmed that the wear tracks had high oxygen content compared to the unworn regions. Thus, WC particles increase the protection on the matrix not only by the virtue of their high elastic modulus and hardness but also by generating the oxides which act as a lubricating layer.

XPS analysis was employed to further understand the worn-out surface composition of the FM MEA and the FM-W10 composite. As shown in Fig. 13, the oxidation reaction occurred on the worn surface of the FM MEA. The spectrum of Fe_{2p} could be fitted into four peaks, which were located at the positions with binding energies of 706.9, 710.6, 720.1, and 724.5 eV (Fig. 13a), which were in good agreement with the standard values of Fe in FeO and Fe_2O_3. Two strong peaks at 640.9 and 652.6 eV could be clearly observed in Fig. 13b, which confirmed the existence of Mn_2O_3. Similarly, Fig. 13c and d confirmed that Cr and Co mainly existed as Cr_2O_3 and CoO. Therefore, the metallic oxides were mainly composed of FeO, Fe_2O_3, Mn_2O_3, Cr_2O_3, and CoO. Also, the metallic oxides (also mainly FeO, Fe_2O_3, Mn_2O_3, Cr_2O_3, and CoO) in Fig. 14 were found in the worn surface of the FM-W10 composite, although no wear particles were visible in Fig. 12b. The XPS result also demonstrated that the FM-W10 composite was oxidized during wear testing. Hence, oxidation wear and abrasion wear were the major wear mechanisms for the FM-W10 composite.

4. Discussion

4.1. *Strengthening mechanisms*

As shown in Table 1, the addition of WC nanoparticles delivered excellent comprehensive mechanical properties. Synergistic effects between WC nanoparticles and $M_{23}C_6$ nanoprecipitates are responsible for the improved properties. In the following sections, the possible strengthening mechanisms that are believed to contribute the improvement of the mechanical properties are discussed separately: (1) load trans-

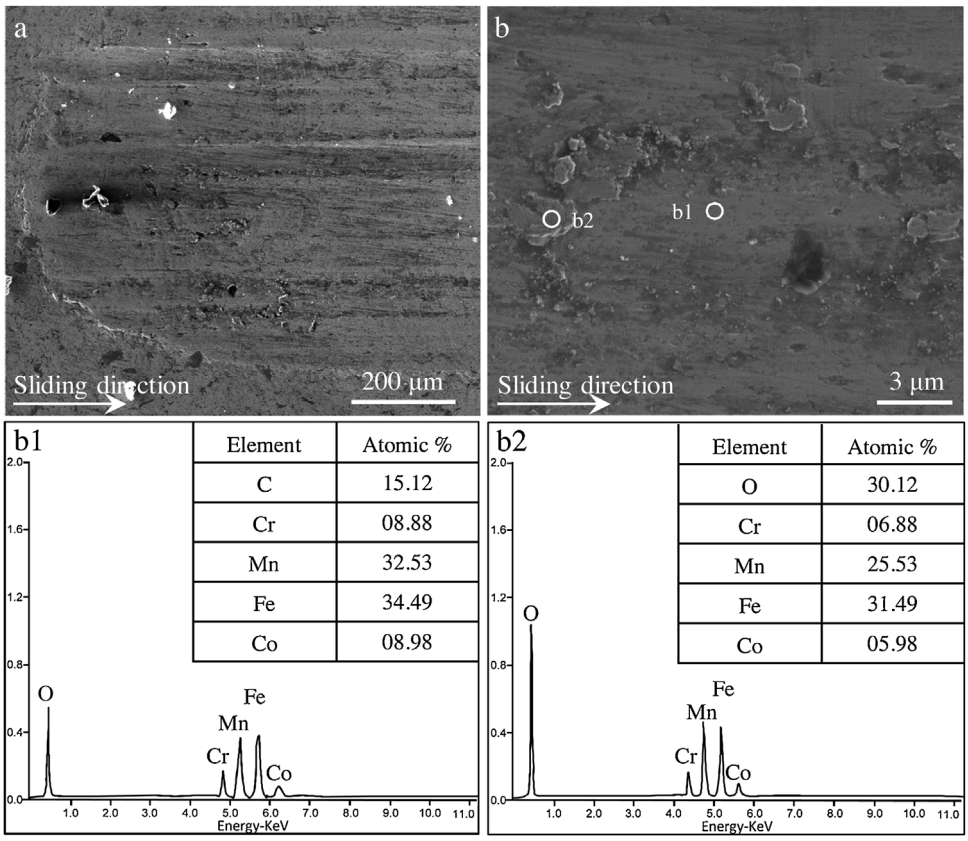

Fig. 11 – (a) SEM micrographs of the wear track on $Fe_{40}Mn_{40}Cr_{10}Co_{10}$ MEA and (b) High magnification SEM image of wear track; (b1) and (b2) corresponding EDS pattern of denoted wear particles in (b).

fer from the FCC matrix to the reinforcements (WC and $M_{23}C_6$), (2) the thermal mismatch mechanism resulting from the generation of dislocations due to the different CTEs between the FCC matrix and the reinforcements; (3) Orowan strengthening mechanism and (4) grain refining caused by pinning effect.

(1) **Load transfer effect.** It is reported that the hardness of WC particles is up to 2200 HV and $M_{23}C_6$ carbides can achieve 1600 HV [55] — higher than the hardness of the FW MEA (320 HV), as shown in Table 1. Therefore, WC and $M_{23}C_6$ are the main carrier phases in this study, working through load transfer from the FCC matrix to the reinforcements during deformation. The improvement in load transfer effect $\Delta\sigma_{LT}$ can be expressed by the following equation [56].

$$\Delta\sigma_{LT}=f_v\sigma_0/2 \quad (1)$$

where f_v denotes the total volume fraction of the WC, and $M_{23}C_6$, σ_0 is the yield strength of the FM MEA. In this work, the value of f_v of WC is 10%, and σ_0 of the FM matrix is 488 MPa. Consequently, the yield strength increment from the load transfer effect of WC is evaluated as 24.4 MPa. Unfortunately, the load transfer effect of $M_{23}C_6$ cannot be calculated, because the volume fraction of $M_{23}C_6$ is not clear.

(2) **Orowan strengthening.** In the present work, the fine WC and $M_{23}C_6$ have a size distribution of a dominant number of particles of less than 600 nm. During deformation, the *ex situ* WC and *in situ* $M_{23}C_6$ act as hard phases at grain boundaries and in the FCC matrix, which interact with dislocations through the pinning effect and block the dislocation movement further (Orowan type). The slip trace within a single grain can move forward when dislocations bypass WC nanoparticles and $M_{23}C_6$ nanoprecipitates. Orowan strengthening can contribute greatly to the improvement in compressive strength for the FM-W10 composites. In this manuscript, unfortunately, the Orowan strengthening effect of $M_{23}C_6$ cannot be calculated, because the volume fraction of $M_{23}C_6$ is difficult to be accurately determined. However, the Orowan strengthening effect of WC only is able to be estimated using Orowan–Ashby equation [57,58].

$$\Delta\sigma\text{Orowan} = 0.13\,Gb/\lambda \ln\frac{D}{2b} \quad (2)$$

$$\lambda = D[(2V_P)^{-1/3}-1] \quad (3)$$

In this study, shear modulus (G) can be calculated as $G=E/2(1+u)$, where u is Poisson's ration (~0.33), and E is the elastic modulus. The value of the elastic modulus for the FM MEA, measured by using the nanoindentation, is 125 GPa. The magnitude of the Burgers vector is $|b|=a_0/\sqrt{2}$, with a_0 being the lattice constant. The average diameter of WC nanoparticles detected by EBSD is 0.54 μm, the volume fraction of WC nanoparticles is 10%, and the lattice constant a_0 detected by XRD is 3.52×10^{-9} nm. Consequently, the yield strength incre-

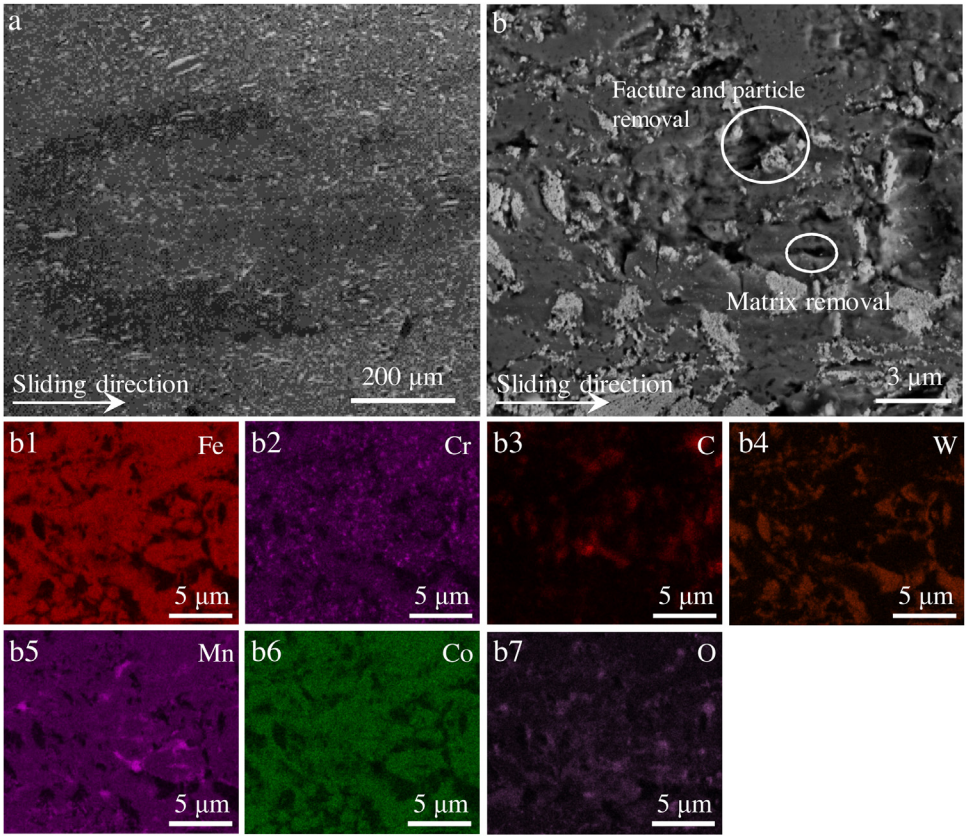

Fig. 12 – (a) SEM micrographs of the wear track on $Fe_{40}Mn_{40}Cr_{10}Co_{10}$/10 vol.% WC composite and (b) High magnification SEM image of wear track; (b1)-(b7) EDS map of worn surface of $Fe_{40}Mn_{40}Cr_{10}Co_{10}$/10 vol.% WC composite based on (b).

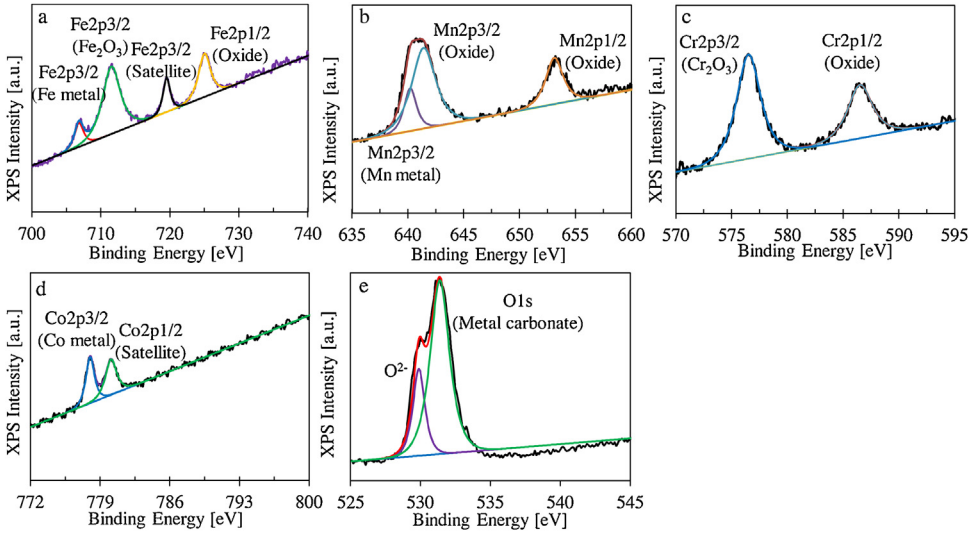

Fig. 13 – The results of XPS analysis of $Fe_{40}Mn_{40}Cr_{10}Co_{10}$ MEA in the air environment. (a) Fe element; (b) Mn element; (c) Cr element; (d) Co element; (e) O element.

ment from Orowan strengthening is estimated to be 27.8 MPa (WC only).

(3) **Thermal mismatch enhancement.** The thermal mismatch mechanism in the composite is bound up with the difference of the coefficient of thermal expansion between the matrix and the reinforcement phase [59,60]. In this study, the CTEs of the $M_{23}C_6$ carbides, WC nanoparticles, and $Fe_{40}Mn_{40}Cr_{10}Co_{10}$ are $1.0–5.0 \times 10^{-6}\,K^{-1}$ [61], $6.9 \times 10^{-6}\,K^{-1}$, and $13 \times 10^{-6}\,K^{-1}$ (refer to FeCoCrNiMn) [62], respectively. Thus, the new thermal mismatch dislocations may be gen-

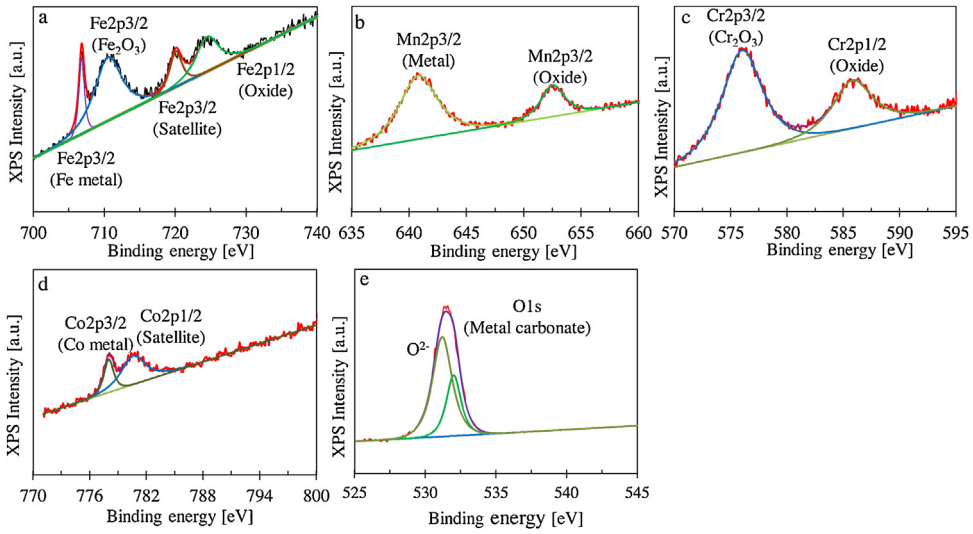

Fig. 14 – The results of XPS analysis of $Fe_{40}Mn_{40}Cr_{10}Co_{10}$/10 vol.% WC composite in the air environment: (a) Fe element; (b) Mn element; (c) Cr element; (d) Co element; (e) O element.

erated at the matrix–WC and matrix–$M_{23}C_6$ interfaces during deformation to relax thermal stresses. TEM results (Fig. 9) show that there were more dislocations at the matrix–WC interface and matrix–$M_{23}C_6$ carbides. These increased dislocations interact with each other, and then impede their own motions and finally increase the resistance to bypass the WC nanoparticles and $M_{23}C_6$ nanoprecipitates. This thermal mismatch eventually leads to the work hardening of materials. The contributions of CTE mismatch strengthening to the yield strength can be expressed as follows [57].

$$\Delta\sigma_{CTE} = \eta G b \rho^{1/2} \tag{4}$$

$$\rho = 12\alpha\Delta T V_P/[bD(1-V_P)] \tag{5}$$

where η is a constant equal to 1.25 [63], and ρ is the enhanced dislocation density. $\Delta\alpha$ is the difference in the CTEs of the matrix ($13\times10^{-6}\,K^{-1}$) and WC ($6.9\times10^{-6}\,K^{-1}$). ΔT is the difference between the processing temperature (solidification temperature of 1100 °C) and the test temperature (25 °C). Thus, the contribution of thermal mismatch (WC nanoparticles) is evaluated as 137.5 MPa. The contribution of $M_{23}C_6$ can also be overlooked because of a similar reason.

(4) **Grain refinement of WC nanoparticles and $M_{23}C_6$ nanoprecipitates.** The EBSD result shows that the grain size of the matrix decreased after adding the WC nanoparticles. The WC nanoparticles and $M_{23}C_6$ nanoprecipitates located at the grain boundaries can bring a strong drag force between two adjacent grains. Then, grain boundary motion can be inhibited by the pinning effect of WC nanoparticles distributing in grain boundaries during sintering, achieving improved mechanical properties. The relationship between yield strength and grain size can be well described by the classical Hall–Petch equation [64,65].

$$\sigma_y = \sigma_0 + k_y/d^{1/2} \tag{6}$$

where k_y is a constant depending on the composites, d is the grain size of the composites, and σ_0 have the same means as defined above. In this work, the value of k_y from the FeCoNiCrMn system, that is, 226 MPa $\mu m^{1/2}$, is used, according to the study of Liu et al. [66]. The average grain sizes of the FCC phase decrease significantly from 4.20 μm (FM MEA) to 1.61 μm (FM-W10) with the increase of the WC nanoparticles. As a consequence, the strength contribution from grain refinement to yield strength is 67.8 MPa. In addition, smaller grain size offers a higher volume fraction of grain boundaries, which could further impede dislocation motion. Both effects are the primary reasons for improving the mechanical properties of the FM-W10 composite by grain refinement. Similar findings were also reported in WC-reinforced Fe alloys [67] and Cu alloys [30].

4.2. *Improvement in friction behavior by adding WC particles*

The results of the tribological test reveal that the addition of WC nanoparticles resulted in a significant increase in tribological properties of the FM-W10 composite, mainly because of the increased hardness of the composite. The FM MEA matrix was more prone to plowing, grooving, and plastic deformation caused by a lower hardness of the matrix and the harder counterpart. As WC and *in situ* $M_{23}C_6$ particles were formed and bonded strongly with the FCC matrix, the tribological properties increased dramatically. Because of the hardness and load-bearing capacity, WC and $M_{23}C_6$ particles can act as plowing stoppers to improve wear. In addition, elemental mapping of worn surface morphology indicates that wear track has high oxygen content in counterpart with the unworn region, WC particles can also improve the friction behavior of the FM-W10 composites by producing oxides that act as lubricating layers. Previous studies have shown that the proper amount of WC and MC-type particles could remarkably improve the tribological properties of the matrix. For example, the tribological properties of Cu alloy were reinforced by WC particles, and the

addition of reinforcing particles enhanced the microhardness and reduced the volume loss, compared with an unreinforced sample [68]. Yuan et al. [69] also found that the friction coefficient and wear rate of the NiAl intermetallic compound significantly decreased by the addition of 30 wt.% WC content. For MC carbide particles, Rainforth et al. [70] found that different carbide sizes can lead to a difference in the wear rate by as much as 40%. Similarly, Luan et al. [71] reported that the wear resistance of a high-speed steel roll is further improved with smaller MC eutectic carbides and uniform distribution in the matrix.

In summary, an interpretation of the results indicates that synergistic effects between WC nanoparticles and $M_{23}C_6$ nanoprecipitates are responsible for improvement in mechanical and tribological properties. In addition, the calculated values of the quantitative contribution from load transfer effect, Orowan strengthening, thermal mismatch enhancement, and grain refinement are 24.4, 27.8, 137.5, and 67.8 MPa, respectively. Thermal mismatch enhancement and the grain refinement are much more effective than other strengthening mechanisms. In addition, the calculated yield strength, 745.5 MPa, is lower than the measured yield strength of 827.5 MPa. The discrepancy may be attributable to two reasons. First, some parameters used for calculation are approximations, or cited from other HEAs. Second, load transfer effects, Orowan strengthening, and thermal mismatch enhancement of $M_{23}C_6$ nanoprecipitates are not calculated, because the volume fraction is not clear. In general, the FM-W10 composite shows excellent mechanical properties because of a good combination of strengthening mechanism, especially thermal mismatch enhancement and grain refinement.

5. Conclusions

Effects of the addition of WC nanoparticles on the microstructure, mechanical and tribological properties of the $Fe_{40}Mn_{40}Cr_{10}Co_{10}$ (FM) medium entropy alloys (MEAs) were investigated. The following conclusions can be drawn:

(a) The addition of WC nanoparticles resulted in the formation of *in-situ* $M_{23}C_6$ precipitates (within grains and along the grain boundaries) in the FM-W10 composite. The formation of nanoprecipitates might not be attributed to the carbon contamination from graphite mold into the MEA during SPS but it is probably owing to the decomposition of WC nanoparticles.

(b) Grain refinement was observed in the FM-W10 composite. The average grain size of the FCC phase decreased from 4.20 to 1.61 μm with the addition of 10 vol.% WC nanoparticles.

(c) The FM-W10 composite exhibited an obvious improvement in mechanical properties with the Vickers hardness of 788 HV, compressive strength of 2.324 GPa, and compressive strain of 33.9%. Load transfer effect, thermal mismatch mechanism, Orowan strengthening mechanism and grain refinement resulted from *ex-situ* WC nanoparticles and *in-situ* $M_{23}C_6$ nanoprecipitates are responsible for the improvement in mechanical properties, especially for thermal mismatch enhancement and grain refinement.

(d) The tribological properties of the FM-W10 composite are superior to those of the FM MEA under the same wear condition. The wear modes of the FM MEA and the FM-W10 composite include the abrasive wear and oxidation wear. Synergistic effects derived from *ex-situ* WC nanoparticles and *in-situ* $M_{23}C_6$ nanoprecipitates are also responsible for the improvement in tribological properties.

Conflicts of interest

The authors declare no conflicts of interest.

Acknowledgments

This project was financially supported by National Natural Science Foundation of China with no. 51404302.

REFERENCES

[1] Yeh JW, Chen SK, Lin SJ, Gan JY, Chin TS, Shun TT, et al. Nanostructured High-En.tropy alloys with multiple principal elements: novel alloy design concepts and outcomes. Adv Eng Mater 2004;6:299–303.
[2] Cantor B, Chang ITH, Knight P, Vincent AJB. Microstructural development in equiatomic multicomponent alloys. Mater Sci Eng A 2004;375-377:213–8.
[3] Bernd G, Anton H, Thurston KVS, Bei H, Wu Z. Exceptional damage-tolerance of a medium-entropy alloy CrCoNi at cryogenic temperatures. Nat Commun 2016;7:10602.
[4] Pogrebnjak AD, Yakushchenko IV, Bagdasaryan AA, Bondar OV. Microstructure, physical and chemical properties of nanostructured (Ti-Hf-Zr-V-Nb)N coatings under different deposition conditions. Mater Chen Phys 2014;147:1079–91.
[5] Pogrebnjak AD, Bagdasaryan AA, Yakushchenko IV. The structure and properties of high-entropy alloys and nitride coatings based on them. Russ Chem Rev 2014;83:1027–61.
[6] Valko N, Kasperovich A, Koltunowicz TN. Forming of a structure of the CoNiFe alloys by the X-ray irradiation. Funct Mater Lett 2018;11:2.
[7] Li Z, Pradeep KG, Deng Y, Raabe D, Tasan CC. Metastable high-entropy dual-phase alloys overcome the strength-ductility trade-off. Nature 2016;534:227–30.
[8] Deng Y, Tasan CC, Pradeep KG, Springer H, Kostka A. Design of a twinning-induced plasticity high entropy alloy. Acta Mater 2015;94:124–33.
[9] Otto F, Dlouhý A, Somsen CH, Bei H, Eggeler G, George EP. The influences of temperature and microstructure on the tensile properties of a CoCrFeMnNi high-entropy alloy. Acta Mater 2013;61:5734–55.
[10] Ganji RS, Karthik PS, Pao KBS, Rajulapati KV. Strengthening mechanisms in equiatomic ultrafine grained AlCoCrCuFeNi high-entropy alloy studied by micro- and nanoindentation methods. Acta Mater 2017;125:58–68.
[11] He JY, Wang H, Huang HL, Xu XD, Chen MW, Wu Y, et al. Precipitation-hardened high-entropy alloy with outstanding tensile properties. Acta Mater 2016;102:187–96.
[12] Liu WH, Lu ZP, He JY, Luan JH, Wang ZJ, Liu B, et al. Ductile $CoCrFeNiMo_x$, high entropy alloys strengthened by hard intermetallic phases. Acta Mater 2016;116:332–42.
[13] Pogrebnjak AD, Beresnev VM. Nanocoatings nanosystems nanotechnologies. Bentham Science Publishers; 2012.

[14] Liu X, Li J, Liu E, Li Q, He C. Effectively reinforced load transfer and fracture elongation by forming Al_4C_3, for in-situ, synthesizing carbon nanotube reinforced Al matrix composites. Mater Sci Eng A 2018;718:182–9.
[15] Arab MS, Mahallawy NE, Shehata F, Agwa MA. Refining SiC_p in reinforced Al-SiC composites using equal-channel angular pressing. Mater Des 2014;64:280–6.
[16] Shi W, Yuan L, Xu F, Zheng Z, Shen D. Refining whisker size of 2024Al/$Al_{18}B_4O_{33}$w composite through extrusion and its effects on the material's micro-structures and mechanical properties. Mater Charact 2018;138:98–106.
[17] Chen B, Shen J, Jia L, Li S. Length effect of carbon nanotubes on the strengthening mechanisms in metal matrix composites. Acta Mater 2017;140:317–25.
[18] Suh YS, Joshi SP, Ramesh KT. An enhanced continuum model for size-dependent strengthening and failure of particle-reinforced composites. Acta Mater 2009;57:5848–61.
[19] Maksakova OV, Simoẽs S, Pogrebnjak AD, Bondar OV, Kravchenko YO. Multilayered ZrN/CrN coatings with enhanced thermal and mechanical properties. J Alloys Compd 2019;776:679–90.
[20] Xiang SL, Hu XS, Wang XJ, Wang LD, Wu K. Precipitate characteristics and synergistic strengthening realization of graphene nanoplatelets reinforced bimodal structural magnesium matrix composites. Mater Sci Eng A 2018;724:348–56.
[21] Liu WH, Yang T, Liu CT. Precipitation hardening in CoCrFeNi-based high entropy alloys. Mater Chen Phys 2018;201:2–11.
[22] Wu L, Li X, Han G, Deng Y, Ma N. Precipitation behavior of the high-Li-content in-situ TiB_2/Al-Li-Cu composite. Mater Charact 2017;132:215–22.
[23] Lai J, Zhang Z, Chen XG. Precipitation strengthening of Al–B_4C metal matrix composites alloyed with Sc and Zr. J Alloys Compd 2013;552:227–35.
[24] Dong XM, Zhang XL, Du K, Zhou YZ, Jin T. Microstructure of carbides at grain boundaries in nickel based superalloys. J Mater Sci Technol 2012;28:1031–8.
[25] Shen M, Tian X, Liu D, Tang H, Cheng X. Microstructure and fracture behavior of TiC particles reinforced Inconel 625 composites prepared by laser additive manufacturing. J Alloys Compd 2018;734:188–95.
[26] Wang JY, Yang HL, Liu ZL, Ji SX, Li RD, Ruan JM. A novel $Fe_{40}Mn_{40}Cr_{10}Co_{10}$/SiC medium-entropy nanocomposite reinforced by the nanoparticles-woven architectural structures. J Alloys Compd 2019;772:272–9.
[27] Cheng H, Chen W, Liu X, Tang Q, Xie Y. Effect of Ti and C additions on the microstructure and mechanical properties of the FeCoCrNiMn high-entropy alloy. Mater Sci Eng A 2018;719:192–8.
[28] Huang G, Hou W, Shen Y. Evaluation of the microstructure and mechanical properties of WC particle reinforced aluminum matrix composites fabricated by friction stir processing. Mater Charact 2018;138:26–37.
[29] Wang J, Li L, Tao W. Crack initiation and propagation behavior of WC particles reinforced Fe-based metal matrix composite produced by laser melting deposition. Opt Laser Technol 2016;82:170–82.
[30] Gu D, Ma J, Chen H, Lin K, Xi L. Laser additive manufactured WC reinforced Fe-based composites with gradient reinforcement/matrix interface and enhanced performance. Compos Struct 2018;192:387–96.
[31] Wan BQ, Sun XY, Ma HT, Feng RF, Li YS. Plasma enhanced chemical vapor deposition of diamond coatings on Cu-W and Cu-WC composites. Surf Coat Technol 2015;284:133–8.
[32] Poblano-Salas CA, Cabral-Miramontes JA, Gallegos-Melgar A, Ruiz-Luna H, Aguilar-Escobar JD, Espinosa-Arbelaez DG. Effects of VC additions on the mechanical properties of bimodal WC-Co HVOF thermal sprayed coatings measured by nanoindentation. Int J Refract Met Hard Mater 2015;48:167–78.
[33] Liu YY, Yu J, Huang H, Xu BH, Liu XL, Gao Y, et al. Synthesis and tribological behavior of electroless Ni-P-WC nanocomposite coatings. Surf Coat Technol 2007;201:7246–51.
[34] Ning K, Ju HF, Bawane K, Lu K. Spark plasma sintering of silicon carbide-nanostructured ferritic alloy composites with chromium carbide barrier layer. Mater Sci Eng A 2007;700:183–90.
[35] Cho S, Kikuchi K, Miyazaki T, Kawasaki A, Arami Y. Epitaxial growth of chromium carbide nanostructures on multiwalled carbon nanotubes (MWCNTs) in MWCNT-copper composites. Acta Mater 2013;61:708–16.
[36] Cutze S, Kuokkala VT. Dependence of tensile deformation behavior of TWIP steels on stacking fault energy, temperature and strain rate. Acta Mater 2010;58:5129–41.
[37] Poletti MG, Fiore G, Gili F, Mangherini D, Battezzati L. Development of a new high entropy alloy for wear resistance: $FeCoCrNiW_{0.3}$ and $FeCoCrNiW_{0.3}$+5at.% of C. Mater Des 2017;115:247–54.
[38] Wang Z, Baker I, Cai Z. The effect of interstitial carbon on the mechanical properties and dislocation substructure evolution in $Fe_{40.4}Ni1_{1.3}Mn_{34.8}Al_{7.5}Cr_6$ high entropy alloys. Acta Mater 2016;120:228–39.
[39] Zhou R, Lin B, Wang JW, Han LL. Microstructures and wear behaviour of $(FeCoCrNi)_{1-x}(WC)_x$ high entropy alloy composites. Int J Refract Met Hard Mater 2018;75:56–62.
[40] Lou D, Hellman J, Luhulima D, Liimatainen J, Lindroos VK. Interactions between tungsten carbide (WC) particulates and metal matrix in WC-reinforced composites. Mater Sci Eng A 2003;340:155–62.
[41] Yu LG, Khor KA, Lia H, Pay KC, Yip TH, Cheang P. Restoring WC in plasma sprayed WC-Co coatings through spark plasma sintering (SPS). Surf Coat Technol 2004;182:308–17.
[42] Li H, Khor KA, Yu LG, Chwang P. Microstructure modifications and phase transformation in plasma-sprayed WC-Co coatings following post-spray spark plasma sintering. Surf Coat Technol 2005;194:96–102.
[43] Kurlov AS, Gusev AI. Tungsten carbides and W-C phase diagrams. Inorg Mater Appl Res 2006;42:121–7.
[44] Machado FAL, Rodrigues MF, Vargas H, Figueira M, Faria RT. Thermal properties of WC–10wt%Co alloys. Mater Res 2008;11:37–41.
[45] Guilemany JM, Paco JMD, Nutting J, Miguel JR. Characterization of the W_2C phase formed during the high velocity oxygen fuel spraying of a WC + 12pct Co powder. Metall Mater Trans 1999;30:1913–21.
[46] Wang X, Guo H, Biest OVD, Vleugels J. Sintering of WC-Co powder with nanocrystalline WC by spark plasma sintering. Rare Met 2006;25:246–52.
[47] Giménez S, Huang SG, Biest OVD, Vleugels J. Chemical reactivity of PVD-coated WC-Co tools with steel. Appl Surf Sci 2007;253:3547–56.
[48] Pascal C, Chaix JM, Doré F, Allibert CH. Design of multimaterial processed by power metallurgy: processing of a (steel/cemented carbides) bilayer material. J Mater Process Technol 2009;209:1254–61.
[49] Rajaei H, Farvizi M, Mobasherpour I, Zakeri M. Effect of spark plasma sintering temperature on microstructure and mechanical properties of mullite-WC composites. Int J Refract Met Hard Mater 2018;70:197–201.
[50] Santodonato LJ, Zhang Y, Feygenson M, Parish CM, Cao MC. Deviation from high-entropy configurations in the atomic distributions of a multi-principal-element alloy. Nature Commun 2015;6:5964.

[51] Lucas MS, Wilks GB, Mauger L, Muñoz JA, Senkov ON. Absence of long-range chemical ordering in equimolar FeCoCrNi. Appl Phys Lett 2012;100:299.
[52] Chou HP, Chang YS, Chen SK, Yeh JW. Microstructure, thermophysical and electrical properties in $Al_xCoCrFeNi$ ($0 \leq \times \leq 2$) high-entropy alloys. Mater Sci Eng B 2009;163:184–9.
[53] Fan QC, Li BS, Zhang Y. The microstructure and properties of (FeCrNiCo)Al_xCu_y high-entropy alloys and their TiC-reinforced composites. Mater Sci Eng A 2014;598:244–50.
[54] Rogal U, Kalita D, Litynska-Dobrzynska L. CoCrFeMnNi high entropy alloy matrix nanocomposite with addition of Al_2O_3. Intermetallics 2017;86:104–9.
[55] Fan C, Chen MC, Chang CM, Wu W. Microstructure change caused by $(Cr,Fe)_{23}C_6$ carbides in high chromium Fe-Cr-C hardfacing alloys. Surf Coat Technol 2006;201:908–12.
[56] Agarwal A, Rao BS, Lahiri D. Carbon Nanotubes Reinforced Metal Matrix Composites. Crc Press 2010.
[57] Chen F, Chen ZN, Mao F, Wang TM, Cao ZQ. TiB_2 reinforced aluminum based in situ composites fabricated by stir casting. Mater Sci Eng A 2015;625:357–68.
[58] Zhang Z, Chen DL. Consideration of Orowan strengthening effect in particulate-reinforced metal matrix nanocomposites: a model for predicting their yield strength. Scr Mater 2006;54:1321–6.
[59] Toropova MM, Steeves CA. Adaptive bimaterial lattices to mitigate thermal expansion mismatch stresses in satellite structures. Acta Astronaut 2015;113:132–41.
[60] Fei WD, Hu M, Yao CK. Thermal expansion and thermal mismatch stress relaxation behaviors of SiC whisker reinforced aluminum composite. Mater Chem Phys 2003;77:882–8.
[61] Chong XY, Jiang YH, Feng J. Exploring the intrinsic ductile metastable Fe-C compounds: complex chemical bonds, anisotropic elasticity and variable thermal expansion. J Alloys Compd 2018;745:196–211.
[62] Laplanche G, Gadaud P, Horat O, Otto F, Eggeler G. Temperature dependencies of the elastic moduli and thermal expansion coefficient of an equiatomic, single-phase CoCrFeMnNi high-entropy alloy. J Alloys Compd 2015;623:348–53.
[63] Liu ZW, Cheng N, Zheng QL, Wu JH, Han QY, Huang ZF, et al. Processing and tensile properties of A356 composites containing in situ small-sized Al_3Ti particulates. Mater Sci Eng A 2018;710:392–9.
[64] Hall EO. The deformation and ageing of mild steel: III discussion of results. Proc Phys Soc 2002;64:747–53.
[65] Petch NJ. The cleavage strength of polycrystals. J Iron Steel Inst 1953;174:25–8.
[66] Liu WH, Wu Y, He JY, Nieh TG, Lu ZP. Grain growth and the Hall–Petch relationship in a high-entropy FeCrNiCoMn alloy. Scr Mater 2013;68:526–9.
[67] Zhang Z, Chen Y, Zuo L, Zhang Y, Qi Y. The effect of volume fraction of WC particles on wear behavior of in-situ WC/Fe composites by spark plasma sintering. Int J Refract Metal Hard Mater 2017;69:196–208.
[68] Cabezas-Villa JL, Olmos L, Vergara- Hernández HJ, Jiménez O, Garnica P. Constrained sintering and wear properties of Cu-WC composite coatings. Trans Nonferrous Met Soc China 2017;27:2214–24.
[69] Yuan J, Zhang X, Li B, Wang X, Sun KJ. Microstructure and tribological behavior of NiAl/WC composites fabricated by thermal explosion reaction at 800°C. J Alloys Compd 2017;693:70–5.
[70] Rodenburg C, Rainforth WM. A quantitative analysis of the influence of carbides size distributions on wear behaviour of high-speed steel in dry rolling/sliding contact. Acta Mater 2007;55:2443–54.
[71] Luan Y, Song N, Bai Y, Kang X, Li D. Effect of solidification rate on the morphology and distribution of eutectic carbides in centrifugal casting high-speed steel rolls. J Mater Process Tech 2010;210:536–41.